

Transient Non-Newtonian Blood Flow under Magnetic Targeting Drug Delivery in an Aneurysm Blood Vessel with Porous Walls

Haleh Alimohamadi¹ and Mohsen Imani²

¹Department of Mechanical Engineering, University of Tehran, Tehran, Iran

²School of Electrical and Computer Engineering, University of Tehran, Tehran, Iran

The present investigation deals with numerical solution of blood flow patterns through an aneurysm artery under the applied magnetic field. Transient extended Navier-Stokes, Brinkman, continuity, and heat conduction equations govern this phenomenon and unsteady pulsatile inlet velocity varies by human heart-beating frequency. Our simulation demonstrates applying 10^5 magnetic field intensity (Mn_F) to recirculate flow and increase fluid flux and maximum blood temperature by 62.5x and 3.5%, respectively, in the aneurysm region. It is also shown that the vessel's wall porosity plays an important role in magnetic targeting of drug delivery performance, as this parameter can noticeably change maximum blood temperature and pressure.

Keywords Biomagnetic fluid, Aneurysm artery, Magnetic nanoparticles, Magnetic targeting drug delivery, Hemodynamic modeling

1. INTRODUCTION

Contemporary drug delivery is done by intravenous injection, where drugs first travel to the heart and then are distributed throughout the body. This method can be inefficient or can damage healthy cells due to the circulation of toxic particles in the body. Magnetic targeting delivery is an efficient and non-destructive new drug delivery method [1, 2]. This method can be employed for many diseases, such as stenosis [3], thrombosis and aneurysms, in order to focus drug particles in specific regions of the blood vessels [4]. Using this method, magnetic field intensity and its gradient in the wish regions should be

powerful enough to return drug particles backward and create concentrated vortexes.

Natural blood has negligible magnetization, and adding solvent ferro nanoparticles is a recent idea for increasing the innate blood magnetization feature. The composition of nanoparticles and fluid is called ferrofluid. This solution can be used in many applications, including electronic, mechanical, bioengineering [5, 6], microstructure [7] and magnetic targeting in porous mediums [8], blood vessels [6, 9], two-phase flow [10], and synovial joints [11, 12].

During the last few decades, numerous investigations have focused on magneto-therapy. The effect of a magnetic field on the efficiency of the drug delivery procedure through the network of blood vessels was studied in [13]. Work on the coupling model of laminar fluid flow by Brinkman and Navier-stokes equations in free and porous media was done in [8]. Dynamic expression for heat and mass transfer in stenosis blood vessels was introduced in [14]. In [15], velocity and temperature distribution of biofluid under the action of external magnetic field were discussed. This article considered the blood artery as a uniform tub with rigid walls. Transient heat transfer of a two-dimensional artery model is detailed in [16] and [17]. However, these papers neglect porous assumption for arterial walls. The effects of permeability, magnetic field, and body acceleration on blood flow patterns passing through a porous media was discussed in [18]. Analytical solution of blood flow considering different viscosity models and in the presence of an external magnetic field was discussed in [19], although this research overlooked the transient essence of this phenomena.

The innovation of our paper is in simulating non-Newtonian blood in double aneurysm geometry and solving transient fluid dynamic equations in coupled free and porous mediums under the action of an external magnetic field. In our work, inlet velocity is considered time-dependent, as the pumping of a real heart and the impact of the external magnetic field are analyzed in different heart cycles. In section 2, the assumed geometry for an

Address correspondence to Haleh Alimohamadi, School of Mechanical Engineering, College of Engineering, University of Tehran, P.O. Box 14395-515, North Kargar St., Tehran, Iran. E-mail: ha.alimohamdi@gmail.com

Color versions of one or more of the figures in the article can be found online at www.tandfonline.com/ucme.

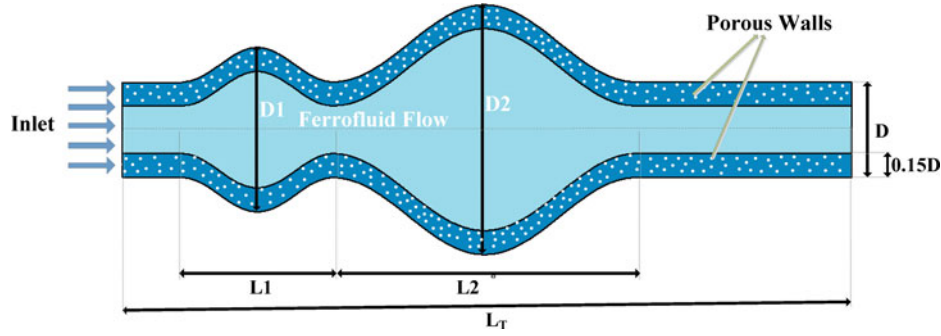


FIG. 1. The geometry model of an aneurysm artery.

aneurysm vessel besides governing equations in both free and porous mediums at the presence of an external magnetic field is discussed. Section 3 presents dimensionless equations and boundary conditions, while simulation results and conclusions are found in sections 4 and 5, respectively.

2. MATHEMATICAL FORMULATION

In this paper, we consider a viscous, non-Newtonian, laminar, incompressible, transient and two-dimensional blood flow through a double-aneurysm geometry. Flow is subjected to external magnetic forces produced by an infinite current plate along the z axis. The geometry of blood vessel with two aneurysms is shown in Fig. 1. The heights of dilations are considered $D1$ and $D2$ and the deformation is represented with two sinuous functions [20]:

$$f(z) = \begin{cases} \left(\frac{D_1 - D}{4} \right) \left[1 + \sin \left(\frac{2\pi x}{L_1} - \frac{\pi}{2} \right) \right] + \frac{D}{2} & 0 \leq x \leq L_1 \\ \left(\frac{D_2 - D}{4} \right) \left[1 + \sin \left(\frac{2\pi(x-L_1)}{L_2} - \frac{\pi}{2} \right) \right] + \frac{D}{2} & L_1 \leq x \leq L_2 \end{cases}$$

The arterial walls are assumed to be porous mediums with $0.15D$ thickness in each side. This assumption brings our model closer to reality because, in real conditions, the inner surface of the vessels' walls is covered with biological materials that mostly have porous characteristics.

2.1 Heat Transfer and Fluid Flow Equations

In our case, two kinds of magnetic forces—magnetization and Lorentz—affect ferrofluid flow. Magnetization appears due to the magnetic field gradient, while the Lorentz force is noticeable because of the high electrical conductivity of ferrofluid. Governing equations on non-Newtonian blood flow under the action of magnetic field are described as below:

Continuity equation:

$$\nabla \cdot \vec{V}^* = 0 \quad (1)$$

Momentum equation [21]:

$$\rho \frac{D\vec{V}^*}{Dt^*} = -\nabla p^* + \eta \nabla^2 \vec{V}^* + \vec{J}^* \times \vec{B}^* + \mu_0 M^* \nabla H^* \quad (2)$$

Energy equation [19]:

$$\rho c_p \frac{DT^*}{Dt^*} + \mu_0 T^* \frac{\partial M^*}{\partial T^*} \frac{DH^*}{Dt^*} - \frac{\vec{J}^* \cdot \vec{J}^*}{\sigma} = k \nabla^2 T^* + \eta \phi \quad (3)$$

where $\vec{V}^* = (u^*, v^*)$ is a two-dimensional velocity field, $\frac{D}{Dt^*} = \frac{\partial}{\partial t^*} + \vec{V}^* \cdot \nabla$ is the material derivative, $\nabla = (\frac{\partial}{\partial x^*}, \frac{\partial}{\partial y^*})$ and $\nabla^2 = \nabla \cdot \nabla = (\frac{\partial^2}{\partial x^{*2}}, \frac{\partial^2}{\partial y^{*2}})$ are Gradient and Laplacian operators, ρ is fluid density, P is pressure, η is dynamic viscosity, μ_0 is magnetic permeability of vacuum, M^* is magnetization, H^* is magnetic field intensity, \vec{B}^* is magnetic induction where $\vec{B}^* =$

TABLE 1
Constant value

Parameters	Numerical value	Parameters	Numerical value
ρ	1050 $kg.m^{-3}$	Ec	8.7×10^{-6}
c_p	$14.65 J.(Kg.K)^{-1}$	α	1.22×10^{-7} $m^2.s^{-1}$
Re	0.23	k	1.832×10^{-3} $Joule.^0$ $K^{-1}m^{-1}s^{-1}$
T_1	$300.^0K$	Mn_F	$[10^5:5 \times 10^5]$
δT	$30.^0K$	Mn_M	150
Pr	4.386	Da	100–400–800
x_1	2	χ_0	0.06
x_2	6	β	$5.6 \times 10^{-3} K^{-1}$
y_0	-0.1	n	0.6
μ_0	$4\pi \times 10^{-7} NA^{-2}$	η_0	$35 \times 10^{-3} kg.m^{-1}.s^{-1}$

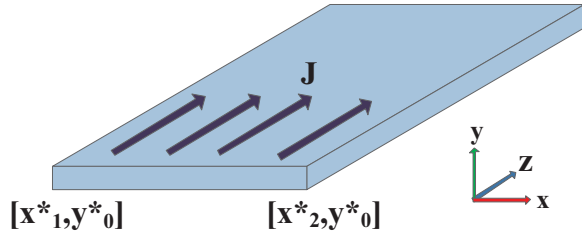


FIG. 2. The plate with current passes through the z direction.

$\mu_0(M^* + H^*)$, σ is electrical conductivity of fluid, J^* is density of electrical current, T^* is temperature, k is thermal conductivity, c_p is specific heat at constant pressure, and ϕ is a dissipation factor that, for a two-dimensional problem, is written as:

$$\phi = 2 \left(\frac{\partial u^*}{\partial x^*} \right)^2 + 2 \left(\frac{\partial v^*}{\partial y^*} \right)^2 + \left(\frac{\partial v^*}{\partial x^*} + \frac{\partial u^*}{\partial y^*} \right)^2 \quad (4)$$

The terms $\mu_0 M^* \nabla H^*$ and $J^* \times B^*$ in the momentum equation demonstrate magnetization and Lorentz forces because of Ferro Hydro Dynamic (FHD) Magneto Hydro Dynamic (MHD) effects. In the energy equation, the terms $\mu_0 T^* \frac{\partial M^*}{\partial T^*} \frac{DH^*}{Dr^*}$ and $\frac{J^* \cdot J^*}{\sigma}$ are added due to magnetization and Joule heating appearance.

In this article, the power law model is used for non-Newtonian ferrofluid viscosity [22]:

$$\eta = \eta_0 |\dot{\gamma}|^n \quad (5)$$

η_0 and n are constant parameters whose values are mentioned in Table 1. $|\dot{\gamma}|$ is the norm of shear rate tensor that for 2D geometry is given as:

$$|\dot{\gamma}| = \left(2 \left(\frac{\partial u^*}{\partial x^*} \right)^2 + 2 \left(\frac{\partial v^*}{\partial y^*} \right)^2 + \left(\frac{\partial u^*}{\partial y^*} + \frac{\partial v^*}{\partial x^*} \right)^2 \right)^{\frac{1}{2}} \quad (6)$$

2.2 Brinkman Equations for Porous Media Flow

In actual conditions, human blood vessels are not rigid and a slight flow can pass through them. Thus, in this article, arterial walls are considered to be porous media. There are various models for the combination of porous and free flow. Among all of these models, Brinkman equations have the best accuracy. Brinkman equations for porous regions are expressed as:

Continuity equation:

$$\nabla \cdot \vec{V}_p^* = 0 \quad (7)$$

Momentum equation:

$$\frac{\rho}{\varepsilon_p} \frac{\partial \vec{V}_p^*}{\partial t^*} = -\nabla p^* + \frac{\eta}{\varepsilon_p} \nabla^2 \vec{V}_p^* - \frac{\eta}{k_{br}} \vec{V}_p^* + J^* \times B^* + \mu_0 M^* \nabla H^* \quad (8)$$

where $\vec{V}_p^* = (u_p^*, v_p^*)$ is the velocity field inside the porous regions. ε_p and k_{br} are porosity and permeability of porous walls. Both magnetization and Lorentz forces are exerted on the porous regions as well, and after obtaining the velocity field in the porous regions, temperature distribution in these domains is calculated by Equation (3).

2.3 Magnetic Formula

For recirculating flow in dilated regions and increasing flow flux into the arterial walls, a powerful external magnetic field has been used. This magnetization is created by a current plate below the bulges and, according to Maxwell's law, it follows the equations:

$$\nabla \times H^* = J = \sigma (\vec{V}^* \times B^*) \quad (9)$$

$$\nabla \cdot B^* = \nabla \cdot (H^* + M^*) = 0 \quad (10)$$

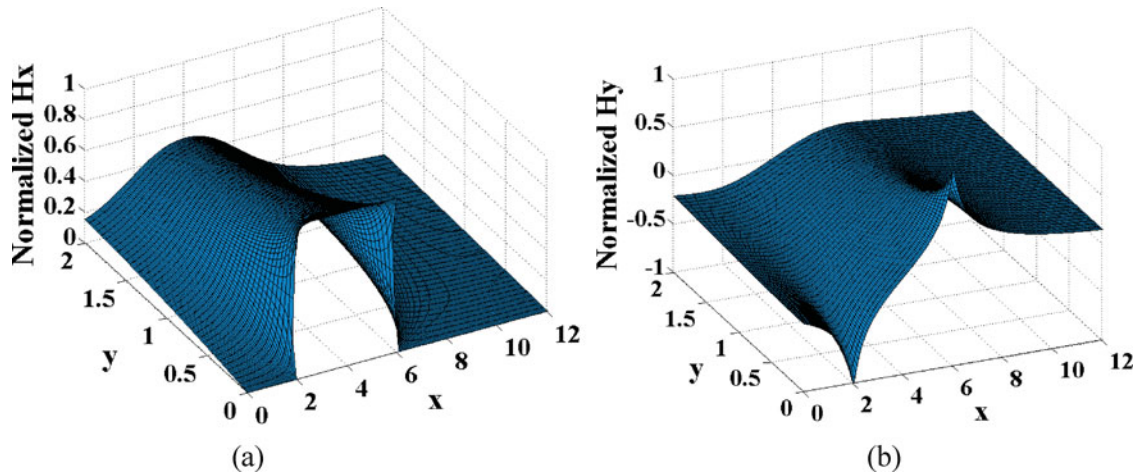


FIG. 3. (a) X-component of normalized total magnetic field intensity; (b) Y-component of normalized magnetic field intensity produced by a current plate.

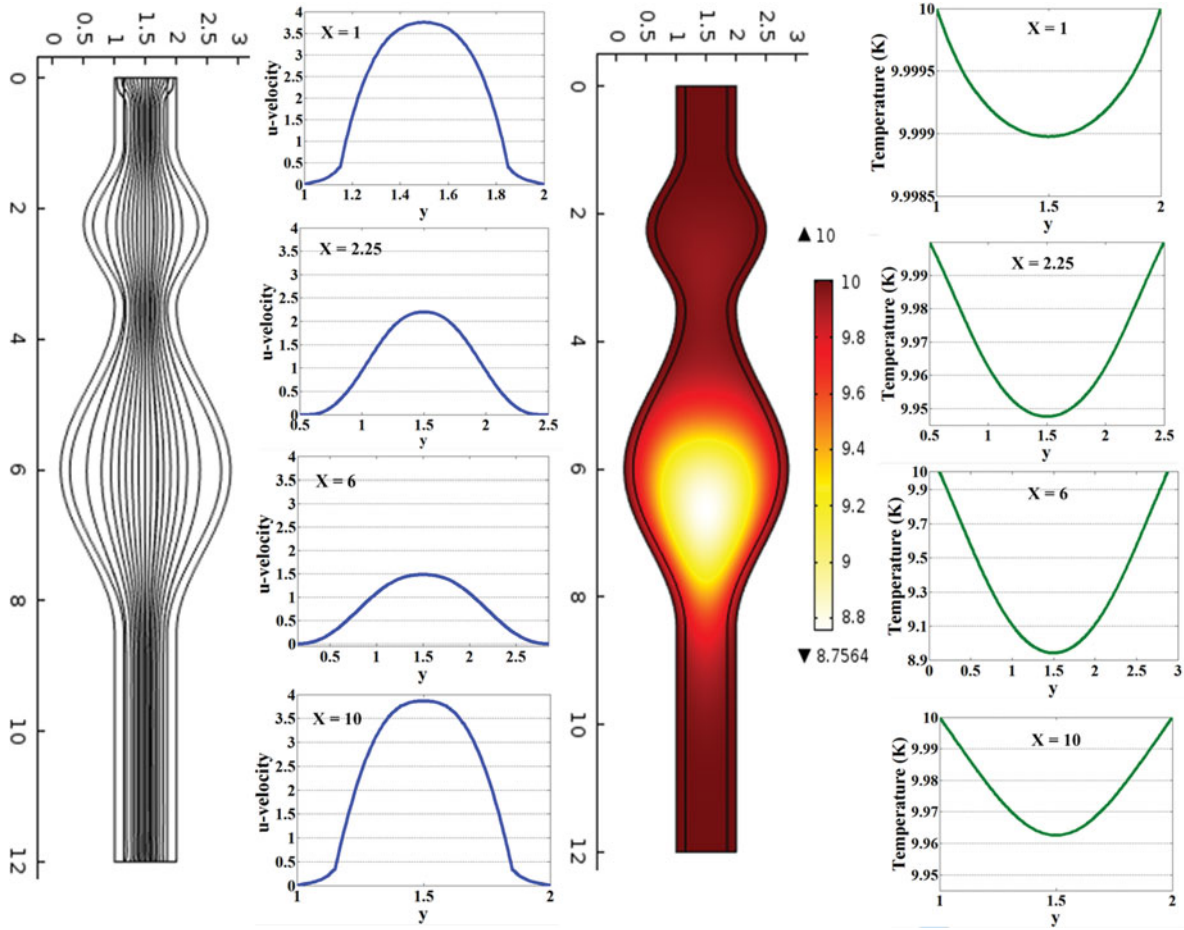


FIG. 4. Stream function and temperature contours with velocity and temperature profiles at time = 1 in different locations.

The magnetic field intensity components (H_x^* , H_y^*) of a current plate is given by:

$$H_y^* = -\frac{H_0}{2} \left[\ln \left(\frac{(x^* - x_2^*)^2 + (y^* - y_0^*)^2}{(x^* - x_1^*)^2 + (y^* - y_0^*)^2} \right) \right] \quad (11)$$

$$H_x^* = H_0 \left[\tan^{-1} \left(\frac{(x^* - x_2^*)}{y^* - y_0^*} \right) - \tan^{-1} \left(\frac{(x^* - x_1^*)}{y^* - y_0^*} \right) \right] \quad (12)$$

$$H^* = \sqrt{H_x^{*2} + H_y^{*2}} \quad (13)$$

H_0 is magnetic field strength which depends on applied magnetization induction ($B = \mu_0 (H+M)$), and x_1^* , x_2^* , y_0^* are the position of the horizontal plate, as shown in Fig. 2. Magnetic field components' distributions in the whole 2D space are shown in Fig. 3. As described earlier, magnetization force consists of multiplying magnetic field and its gradient in different points of space. Thus, magnetic force is severely high in the edges of the plate. This force can affect ferrofluid flow and divert it from direct motion. The X-component of this force wants to stop fluid motion and return it backward, while the Y-component drags particles upwards and to the circulating flow inside the bulges.

2.4 Magnetization Equation

The impression of magnetic field on the flow is determined by the magnetization property (M^*), which is an innate characteristic of the ferrofluid. This feature is modeled with numerous equations but, in this article, the linear formula which relates magnetization to magnetic field strength and temperature is used [23]:

$$M^* = \chi_m H^* \quad (14)$$

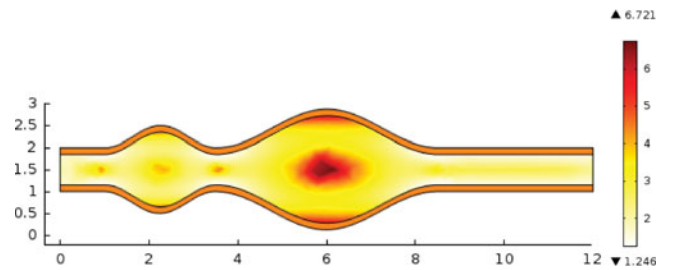


FIG. 5. The viscosity contour in the aneurysm vessel model without considering magnetization effect at time = 1.

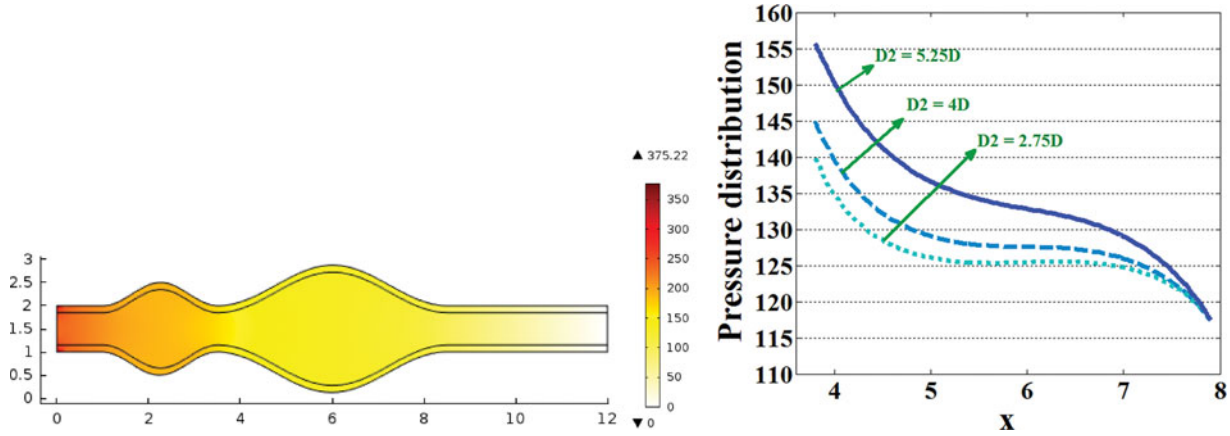


FIG. 6. Pressure contour and its distribution on the second bulge place versus variation on its size at time = 1.

χ_m is the magnetic susceptibility and varies with temperature:

$$\chi_m = \frac{\chi_0}{1 + \beta(T^* - T_0)} \quad (15)$$

χ_0 , β and T_0 are constant parameters that are obtained by experimental research [23].

3. TRANSFORMATION OF EQUATIONS

In order to solve the coupled systems of equations, it is convenient to introduce the following non-dimensional variables:

$$t = \frac{\alpha}{D^2} t^*, \quad x = \frac{x^*}{D}, \quad y = \frac{y^*}{D}, \quad u = \frac{u^*}{u_r}, \quad v = \frac{v^*}{u_r}, \quad p = \frac{p^*}{\rho u_r^2} \quad (16)$$

$$H = \frac{H^*}{H_0}, \quad T = \frac{T^*}{\delta T}$$

where $\alpha = \frac{K}{\rho c_p}$ is thermal diffusivity of the fluid and $u_r = \frac{\alpha}{D}$ is defined characteristic velocity.

By substituting theses non-dimensional variables into Equations (1)–(8) and (15), we have:

In free flow:

Continuity:

$$\frac{\partial u}{\partial x} + \frac{\partial v}{\partial y} = 0 \quad (17)$$

x-momentum:

$$\frac{\partial u}{\partial t} + u \frac{\partial u}{\partial x} + v \frac{\partial u}{\partial y} = -\frac{\partial p}{\partial x} + \text{Pr} \times |\dot{\gamma}^*| \left(\frac{\partial^2 u}{\partial x^2} + \frac{\partial^2 u}{\partial y^2} \right) + Mn_F \chi_m H \frac{\partial H}{\partial x} + \frac{Mn_M}{\text{Re}} (\chi_m + 1)^2 (v H_x H_y - u H_y^2) \quad (18)$$

y-momentum:

$$\frac{\partial v}{\partial t} + u \frac{\partial v}{\partial x} + v \frac{\partial v}{\partial y} = -\frac{\partial p}{\partial y} + \text{Pr} \times |\dot{\gamma}^*| \left(\frac{\partial^2 v}{\partial x^2} + \frac{\partial^2 v}{\partial y^2} \right) + Mn_F \chi_m H \frac{\partial H}{\partial y} + \frac{Mn_M}{\text{Re}} (u H_x H_y - v H_x^2) \quad (19)$$

Also, the energy equation is rewritten as Equation (20):

$$\begin{aligned} \frac{\partial T}{\partial t} + u \frac{\partial T}{\partial x} + v \frac{\partial T}{\partial y} = & \left(\frac{\partial^2 T}{\partial x^2} + \frac{\partial^2 T}{\partial y^2} \right) + Ec \times \text{Pr} \times |\dot{\gamma}^*| \\ & \left(2 \left(\frac{\partial u}{\partial x} \right)^2 + 2 \left(\frac{\partial v}{\partial y} \right)^2 + \left(\frac{\partial v}{\partial x} + \frac{\partial u}{\partial y} \right)^2 \right) \\ & - Mn_F \times Ec \times \frac{\partial \chi}{\partial T} T \times H \left(u \frac{\partial H}{\partial x} + v \frac{\partial H}{\partial y} \right) + \frac{Mn_M}{\text{Re}} \\ & \times Ec \times (\chi_m + 1)^2 \times (u H_y - v H_x)^2 \end{aligned} \quad (20)$$

For the porous region, continuity and energy equations are similar to free-flow medium, but momentum equations are:

x momentum:

$$\begin{aligned} \frac{\partial u_p}{\partial t} = & -\frac{\partial p}{\partial x} + \text{Pr} \times |\dot{\gamma}^*| \left(\frac{\partial^2 u_p}{\partial x^2} + \frac{\partial^2 u_p}{\partial y^2} \right) + \text{Pr} \times Da \times u_p + \\ & Mn_F \times \chi_m \times H \frac{\partial H}{\partial x} + \frac{Mn_M}{\text{Re}} (\chi_m + 1)^2 (v_p H_x H_y - u_p H_y^2) \end{aligned} \quad (21)$$

y momentum:

$$\begin{aligned} \frac{\partial v_p}{\partial t} = & -\frac{\partial p}{\partial y} + \text{Pr} \times |\dot{\gamma}^*| \left(\frac{\partial^2 v_p}{\partial x^2} + \frac{\partial^2 v_p}{\partial y^2} \right) + \text{Pr} \times Da \times v_p + \\ & Mn_F \chi_m H \frac{\partial H}{\partial y} + \frac{Mn_M}{\text{Re}} (u H_x H_y - v H_x^2) \end{aligned} \quad (22)$$

where

$$|\dot{\gamma}^*| = \left(2 \left(\frac{\partial u}{\partial x} \right)^2 + 2 \left(\frac{\partial v}{\partial y} \right)^2 + \left(\frac{\partial u}{\partial y} + \frac{\partial v}{\partial x} \right)^2 \right)^{\frac{n-1}{2}} \quad (23)$$

$$\chi_m = \frac{\chi_0}{1 + (\beta \delta T)(T - \frac{T_0}{\delta T})} \quad (24)$$

The non-dimensional parameters which appear in these equations are:

$$\text{Re} = \frac{D \rho u_r}{\eta_0 \times \left(\frac{\alpha}{D^2} \right)^{-0.4}}$$

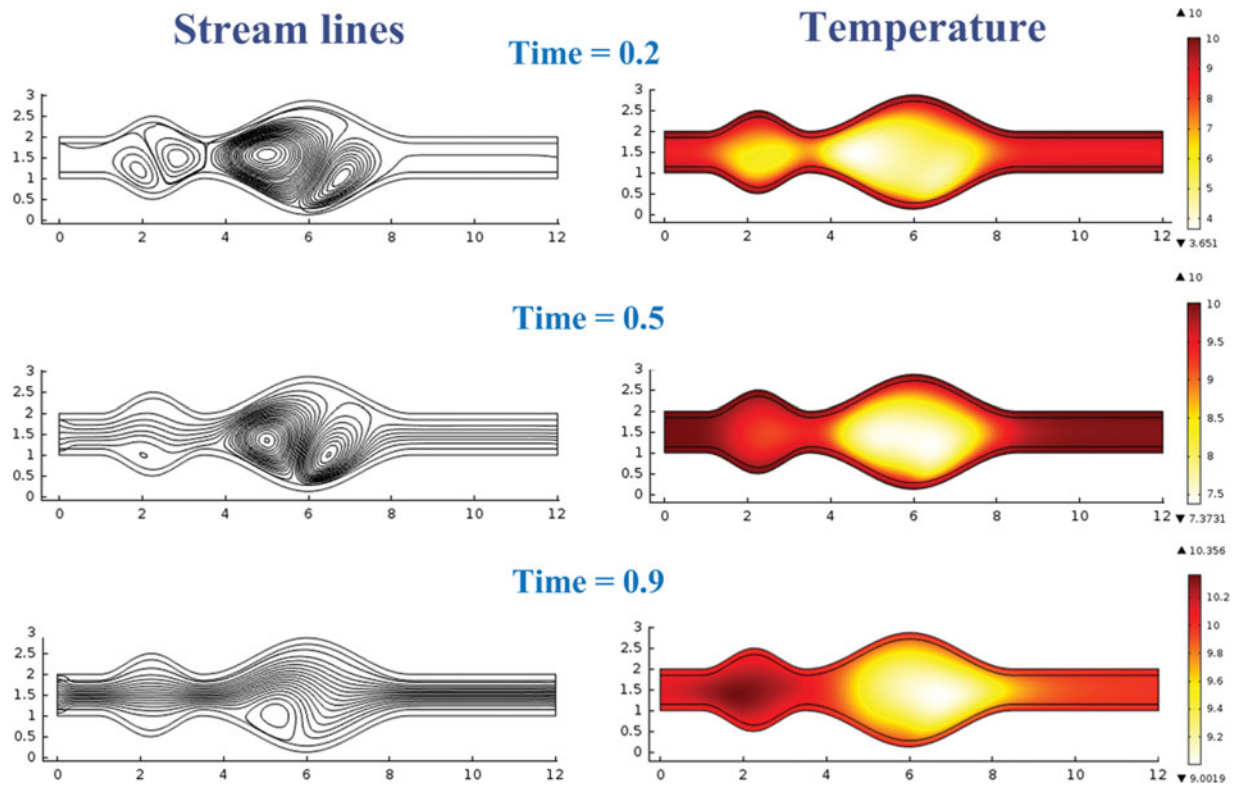


FIG. 7. Stream functions and temperature contours with $Mn_F = 10^5$ and $Mn_M = 10^2$ in different time steps.

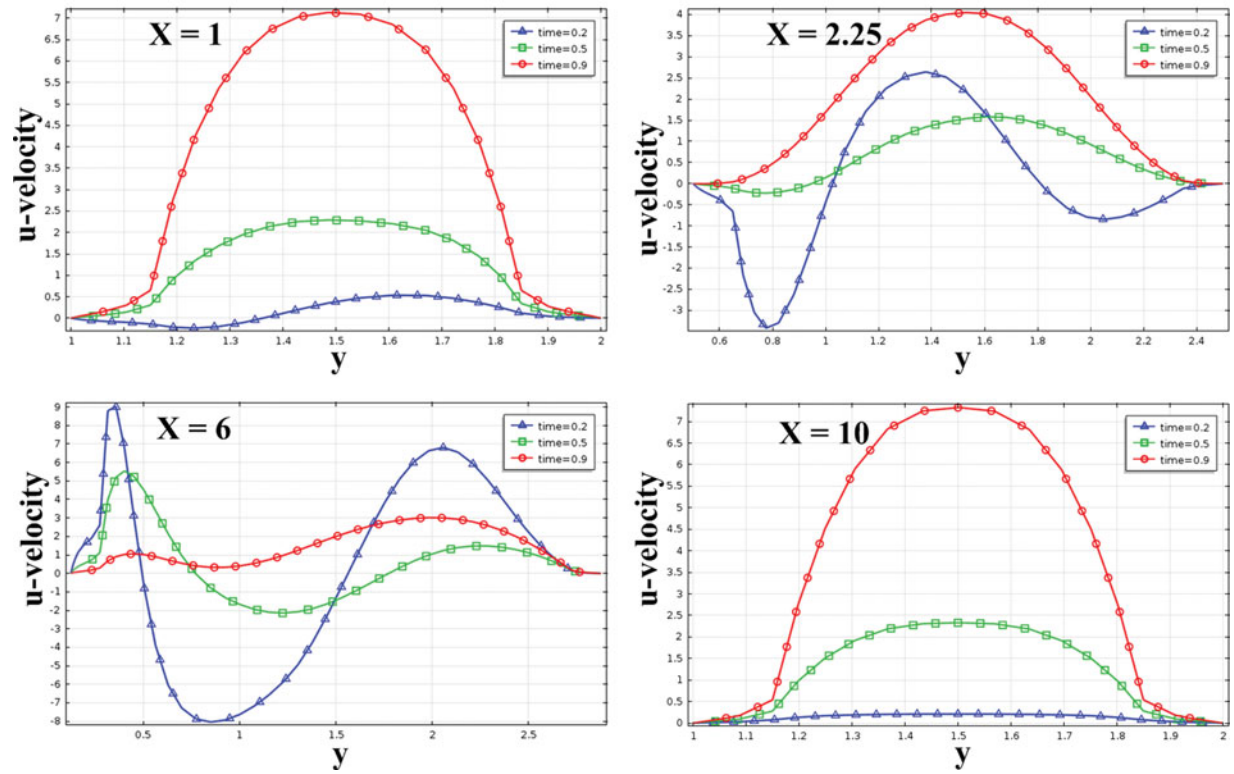


FIG. 8. The time variation of velocity profile in different x -positions with $Mn_F = 10^5$ and $Mn_M = 10^2$.

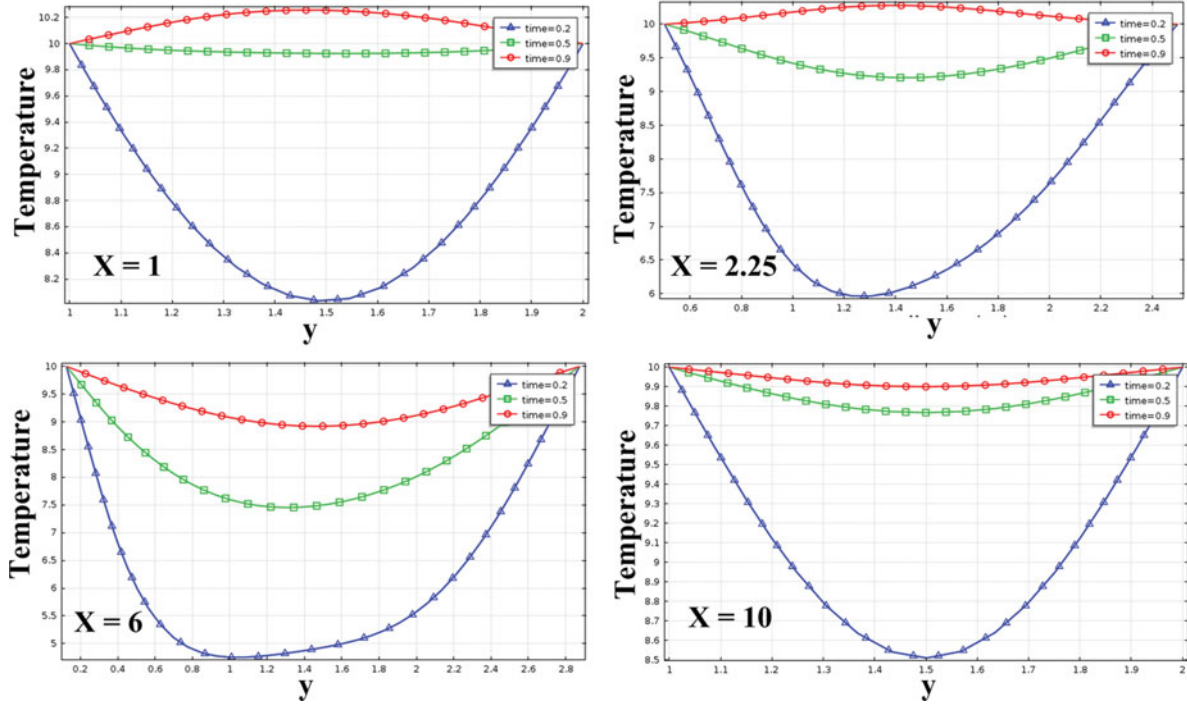


FIG. 9. The time variation of temperature profile in different x positions with $Mn_F = 10^5$ and $Mn_M = 10^2$.

$$= \frac{\rho\alpha}{\eta_0 \times (\frac{\alpha}{D^2})^{-0.4}} \text{ (Reynolds number)} \quad (25)$$

$$Ec = \frac{u_r^2}{C_p \delta T} = \frac{\alpha^2}{C_p \delta T D^2} \text{ (Eckert number)} \quad (26)$$

$$Pr = \frac{\eta_0 \times (\frac{\alpha}{D^2})^{-0.4}}{\rho\alpha} \text{ (Prandtl number)} \quad (27)$$

$$Da = \frac{D^2}{k_{br}} \text{ (Darcy number)} \quad (28)$$

$$Mn_F = \frac{\mu_0 H_0^2}{\rho u_r^2} = \frac{\mu_0 H_0^2 D^2}{\rho \alpha^2} \text{ (Magnetic number of FHD)} \quad (29)$$

$$Mn_M = \frac{\mu_0^2 H_0^2 D^2 \sigma}{\eta} \text{ (Magnetic number of MHD)} \quad (30)$$

3.1 Boundary Conditions

The implemented non-dimensional boundary conditions for solving Equations (17)–(22) are:

- Upper plate: $y = 1$ and $0 < x < 12$:
 $T = T_1$, $u = v = 0$
- Lower plate: $y = 0$ and $0 < x < 12$:
 $T = T_1$, $u = v = 0$
- Outlet: $x = 12$ and $0 < y < 1$:
 $\frac{\partial T}{\partial x} = 0$, $p = 0$
- Inlet: $x = 0$ and $0 < y < 1$:
 $T = T_1$ and the axial transient uniform flow is entered into the artery as [24]. This is the exact inlet velocity of blood

vessels which is observed from the experimental tests.

- For the free-porous interface, it is assumed that velocity is equal in these two regions ($\vec{V}_p = \vec{V}$). This assumption satisfies the continuity condition of the velocity field between free and porous mediums [25].

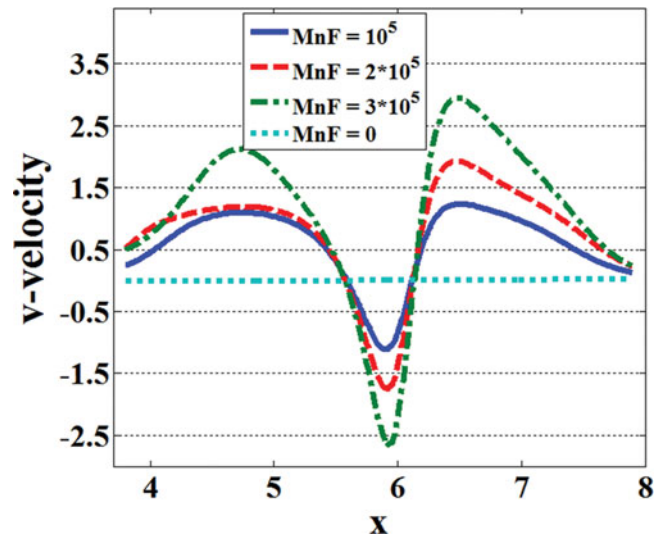


FIG. 10. “V” velocity profile in the aneurysm region with different magnetic field intensities at time = 0.2.

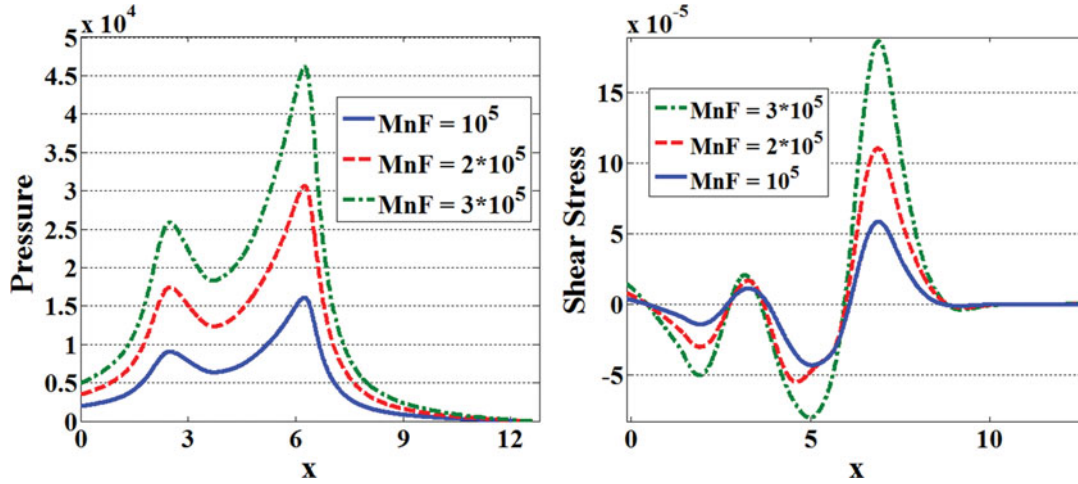


FIG. 11. Shear stress and pressure distribution on the lower wall with different values of magnetic field intensity and $Mn_M = 10^2$ at $t = 0.2$.

4. SIMULATION RESULT

The time-dependent flow in the described geometry is solved using COMSOL 4.3 Multiphysics software and with a free and porous media flow toolbox. The constant values that are used in this article are described in Table 1 [15, 17].

4.1 Flow in Aneurysm Artery Without Magnetic Force

In this article, aneurysm region length is assumed to be smaller than the total length of the vessel. Thus, uniform inlet velocity and output flow from the second dilation quickly reach a fully developed condition. Laminar flow streamlines and temperature contour at time = 1 are shown in Fig 5. Because of the low Reynolds number ($Re = 0.23$) at the entrance, there is no separation and all of the artery and dilations are filled with fluid streams in the forward direction. As the “u” velocity component graph in specific locations indicates, deceleration and acceleration fluid flow inside the double-aneurysm model result in very low axial velocity in dilations; in the second bulge, maximum dimensionless axial velocity is about 1.5, while in the fully developed regions the inner core of flow moves 2.5 times faster. As expected, due to the porous assumption for the upper and lower walls, velocity magnitude in these regions is much lower than in other locations. As shown in Fig. 6, the second bulge has the lowest temperature (about 1.2K below the sur-

face temperature) because, in this region, the cross-sectional area expands, and consequently, both velocity and temperature magnitude decline.

Viscosity variation through the two-aneurysm model at time = 1 is shown in Fig. 5. This figure elucidates the highest viscosity of fluid at the middle of the larger dilation. Because, by entering the jet of fluid into the expanded area, flow decelerates sharply, shear rate term in the non-Newtonian power law model and, consequently, viscosity value rise remarkably.

Along the length of the artery, fluid pressure decreases gradually until it reaches zero value at the outlet section. The maximum, minimum, and rate of pressure reduction depend on the size of the aneurysm. As Fig. 6 shows, by enlarging the second bulge dimension, both pressure magnitude and its gradient increase by doubling the aneurysm diameter from 2.75D to 5.25D, and almost 11% higher pressure is exerted on the surface [20].

4.2 Time-Dependent Effect of Magnetization on Biofluid

Stream function and temperature contours in the presence of an external magnetic field at three different times ($t = 0.3, 0.5, 0.9$) are demonstrated in Fig. 7. Magnetic forces push fluid flow in a reversed direction and, as a result, two groups of vortexes are formed and occupy all of the two aneurysms’ sac volume. In

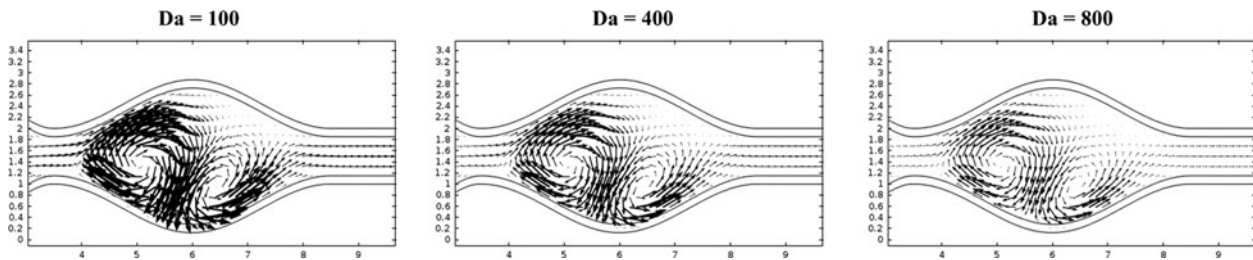


FIG. 12. Velocity arrows in the artery with different Darcy numbers ($Da = 100, 400$ and 800) with $Mn_M = 10^2$ - $Mn_F = 10^5$ at time = 0.2

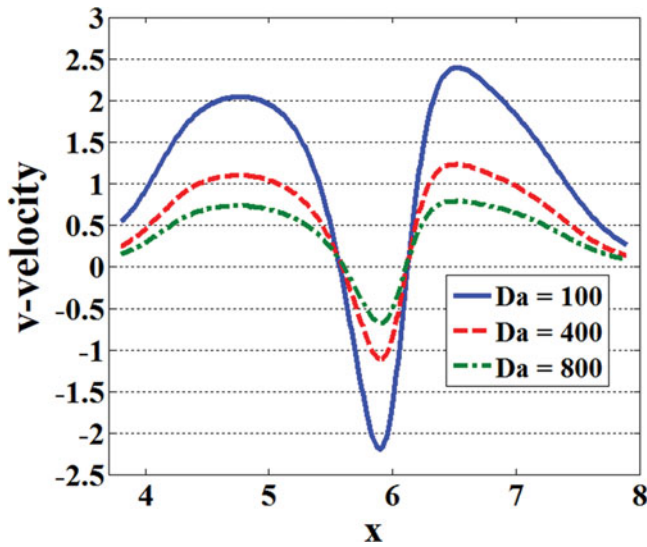


FIG. 13. “V” velocity in the aneurysm region with different Darcy numbers and $Mn_F = 10^{-5}$, $Mn_M = 10^2$ at time = 0.2.

each vortex group, the first vortex rotates clockwise while the second one revolves counterclockwise. At $t = 0.2$, inlet axial velocity is negative (see Fig. 4) and all magnetic, viscous, and inertia forces applied to the fluid move in the same direction, so two big whirlpools are created in each bulge. With time, the inlet velocity becomes positive and viscosity and inertia forces try to attenuate the effect of exerted magnetic forces. This domination continues until $t = 0.5$, when the vortexes in the smaller bulge disappear completely, and finally, at $t = 0.9$, the viscous and inertia forces overcome the magnetic forces entirely and only a small whirlpool remains in the larger aneurysm. These vortexes are useful for creating stagnant ferrofluid flow in the target site and allowing drug carriers to concentrate on a specific location. The temperature contours in this figure demonstrate, through the passage of time, that blood temperature rises such that, at $t = 0.9$, the first bulge temperature becomes 0.2 K higher than the arterial walls. During the application of the external magnetic field, although the temperature of larger dilation is always below the arterial walls’ temperature, with the presence of the magnetic field, the final temperature of blood at time = 0.9 increases almost 4.5%, rather than the simple case without

TABLE 2

Time variation of Nusselt number on the lower wall in a different magnetic field with $Mn_M = 10^2$

Time	Mn_F					
	0	10^5	2×10^5	3×10^5	4×10^5	5×10^5
0.2	2.289	2.641	2.549	2.579	2.609	2.598
0.4	0.744	0.679	0.621	0.585	0.551	0.508
0.6	0.257	0.175	0.115	0.071	0.034	-0.0007
0.8	0.088	-0.028	-0.129	-0.215	-0.289	-0.354
1	-0.024	-0.142	-0.290	-0.415	-0.517	-0.598

magnetization. In fact, embedding and using a current plate to act as a heat source increases blood temperature, particularly in the dilated regions. This temperature increment can be useful in drug absorption, since some drugs need warm ambient for activation; thus, using an external magnetic field is an efficient and non-destructive way to expediting drug absorption on a target area.

Time variations of the dimensionless axial velocity (“u”) in the presence of an external magnetic field for a specific location are depicted in Fig. 8. Location $x = 1$ is far from the current plate, and the effect of formed vortexes is less than in other areas; the velocity profile only varies by changes of inlet velocity. At the middle of the smaller dilation ($x = 2.25$), the created vortexes at $t = 0.2$ reinforce reverse flow along the vessel, but with time, the impact of these vortexes dwindles and the velocity profile returns back to its former, fully developed profile (see Fig. 5). At $x = 6$, the formed vortexes have strongly attenuated positive flow, reversed the inner core fluid flow, and lasted longer (until $t = 0.9$). Location $x = 10$ is far from both vortexes and the impact of the transient inlet velocity such that the axial velocity in this cross-section acts as a fully developed profile. Time-variant temperature configuration at different locations is shown in Fig. 9. As this figure shows, with the passage of time, blood temperature increases in all locations, but at $x = 2.25$, inside the smaller dilation, this increment is maximized and fluid temperature reaches 0.2 K higher than the arterial walls.

TABLE 3

Effect of porosity value on maximum velocity and temperature with different percent of artery aneurysm and $Mnf = 10^5$, $Mn_M = 10^2$ at time = 1

D_2/D	2.75			4			5.25		
Darcy Number	$P_{max} \times 10^3$	T_{max}	μ_{max}	$P_{max} \times 10^3$	T_{max}	μ_{max}	$P_{max} \times 10^3$	T_{max}	μ_{max}
100	17.476	10.351	5.413	22.174	10.205	5.5526	42.237	10.113	7.047
400	17.516	10.368	5.254	22.217	10.211	5.295	42.274	10.117	6.868
800	17.530	10.376	5.162	22.227	10.223	5.272	42.284	10.121	6.6062

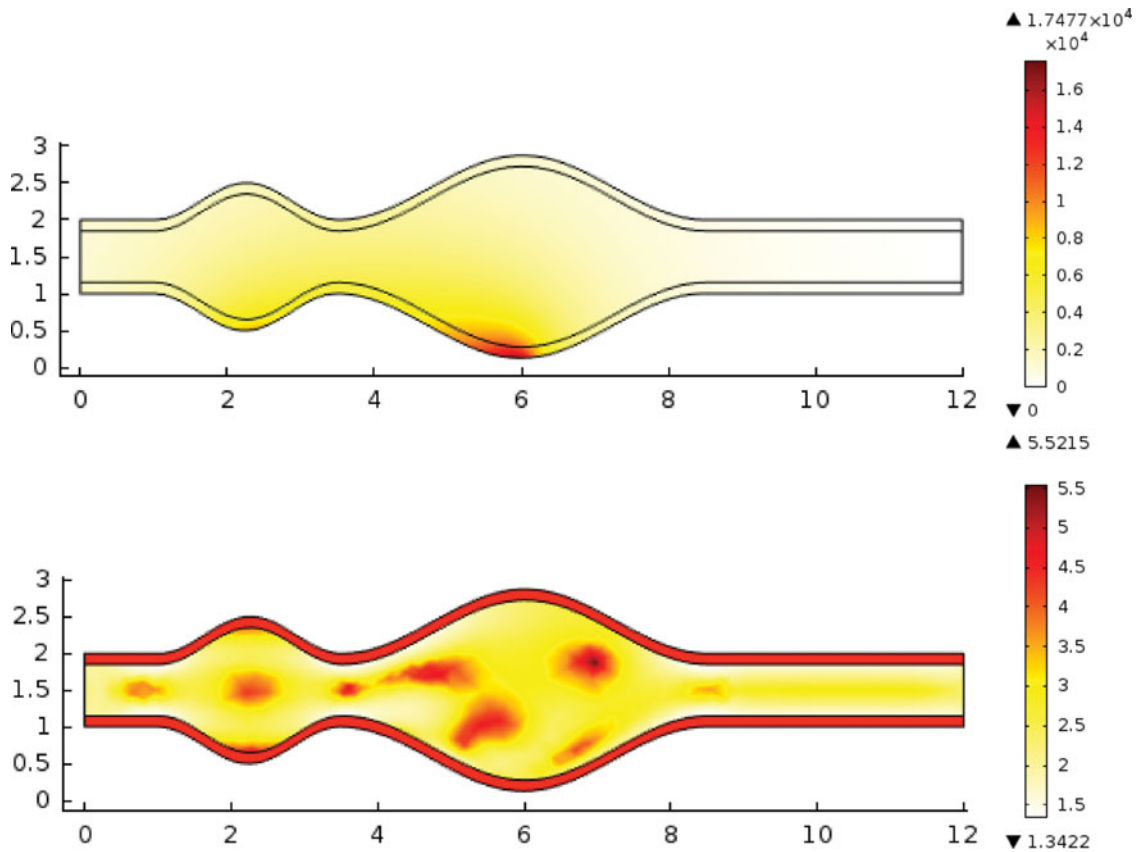


FIG. 14. Pressure and viscosity counter inside the artery with $Da = 100$, $Mn_F = 10^5$, $Mn_M = 10^2$ at $t = 1$.

4.3 Effect of Magnetic Field Intensity on Fluid Flow

Magnetic field intensity has a direct impact on penetration velocity, temperature, pressure and shear stress distribution. The effect of this parameter on the “v” velocity component along the larger aneurysm is shown in Fig. 10. As seen, with the presence of an external magnetic field, blood flow gets velocity in the “y” direction and is pushed downward strongly at the middle of the dilatation (negative vertical velocity). This occurrence provides an appropriate condition for the drug carrier to become stagnant above the swollen area and to be absorbed more easily. We also can expedite this process by strengthening the applied magnetic field (in this case, doubling and tripling magnetic field intensity from 10^5) because vertical flux to the dilatation section goes up noticeably (increases to about 1.65x and 1.6x, respectively).

Shear stress and pressure distribution on the lower arterial wall versus magnetic field intensity are shown in Fig. 11. Vortex formation and expanding cross-sectional area in the smaller dilatation influence upstream flow in the entire straight artery section. By entering smaller dilatation, wall pressure starts to increase and, at the middle of dilatation, it reaches its maximum value. After the apex point, pressure magnitude falls suddenly because flow enters into a converging nozzle and accelerates quickly. In the second step, flow encounters a larger bulge and

the wall pressure rises again, but this increment occurs more sharply, since maximum pressure in the larger dilatation is about two times higher than in the smaller one. Finally, after the second peak in the larger dilatation, wall pressure magnitude drops abruptly and approaches zero set value at the existence.

Shear stress variation on the lower wall in Fig. 11 demonstrates that flow recirculation and deceleration in the dilated regions produce negative velocity gradient in the vicinity of the lower wall as far as levorotatory shear force is exerted to approximately half of both bulges’ surfaces. In the middle of each dilatation (almost at $x = 2.5$ and $x = 6$), shear stress becomes zero, its sign changes and increases in a positive direction until it attains its maximum value. After this point, flow enters into the distal areas and, because of geometry compulsion for straightening streamlines, shear stress value declines sharply. According to this figure, larger dilatation tolerates higher absolute shear stress, such that in the positive and negative directions, it must bear 9.1 times and 1.7 times higher stress than the smaller bulge (with $Mn_F = 10^5$). By strengthening magnetic field intensity, bigger and more powerful vortices influence a wider area. By applying a magnetic field that is twice as strong as $Mn_F = 10^5$, maximum fluid shear stress and pressure in the second dilatation will become 2.1x and 1.9x higher.

According to our simulation, in normal conditions and without the presence of an external magnetic field, ferrofluid temperature is lower than in the arterial walls and heat transfers from wall to fluid at the first time steps. However, with time, the biofluid becomes warmer and heat transfer direction is reversed. This occurrence is shown in Table 2, where the Nusselt number varies from a positive to negative value with time. However, by applying magnetic forces and increasing its intensity, the heat transfer rate goes up noticeably and ferrofluid temperature becomes dominant in fewer time steps.

4.4 Effect of Porosity on Magnotherapy Performance

Darcy number signifies porous permeability of the arterial walls; the effect of this parameter on the vortex power and vertical velocity in the larger dilation is illustrated in Fig. 12 and Fig. 13. Based on these figures, by decreasing the Darcy number value, bigger and stronger vortexes are created inside the bulge, and quartering this parameter from 400 to 100 results in 2.2 times' higher fluid flux into the dilation's wall. Thus, we can conclude that vessels with lower Darcy number magnitude (more porosity feature) can be treated better in a magnetotherapy process since, in these vessels, a weak magnetic field is powerful enough to produce vortexes, accumulate drug carrier in the target site, and provide a suitable condition for their efficient absorption.

Table 3 shows maximum pressure, temperature, and viscosity for different porosity factors and the second dilation diameter. It is shown that increasing both the Darcy number and dilation diameter raise the maximum blood pressure in the whole artery. In the presence of the external magnetic field, maximum blood pressure occurs inside the lower porous wall (Fig. 14), and by increasing Darcy number value and dilation diameter, flow deceleration in the porous region increases maximum blood pressure remarkably, such that in each Darcy number, by doubling dilation diameter, maximum pressure becomes two times higher. Moreover, increasing the Darcy number makes the porous regions more solid and flow passage harder, so that reduction in the available cross-sectional area produces higher maximum velocity and, consequently, higher maximum blood temperature. This velocity increment decreases maximum blood viscosity because, based on Fig. 14, maximum viscosity occurs in bigger dilation. At constant dilation diameter ($D_2 = 2.75D$), increasing the Darcy number from 100 to 800 enhances and weakens maximum blood temperature viscosity by about 0.25% and 4.6%, respectively. On the other hand, as it seen in Table 3, by doubling the dilation diameter in the constant Darcy number ($Da = 100$), maximum blood temperature drops approximately 2.5% while maximum viscosity goes up about 30%.

5. CONCLUSION

This article discusses the transient effect of external magnetic field on the double-aneurysm blood vessel with porous medi-

ums on the walls. Blood flow is considered as a non-Newtonian biofluid and, in order to create vortexes in each bulge, an infinite current plate is fixed under the dilatations. The flow recirculation provides the appropriate condition and time for drug carriers to aggregate at the target region. Also, the applied magnetic field increases fluid flux and temperature on the aneurysm regions, which expedites drug penetration and activation in the diseased section. The present simulation shows that vessels with higher porous walls have better performance in magnetic drug targeting treatment because, in this case, one weak magnetic field can make big enough vortexes and dominate the entire vessel domain.

REFERENCES

1. C. Alexiou, W. Arnold, R.J. Klein, F.G. Parak, P. Hulin, C. Bergemann, W. Erhardt, S. Wagenpfeil, and A.S. Luebbe, Locoregional Cancer Treatment with Magnetic Drug Targeting, *Cancer Research*, vol. 60, pp. 6641–6648, 2000.
2. C. Alexiou, R. Jurgons, R. Schmid, W. Erhardt, F. Parak, C. Bergemann, and H. Iro, Magnetic Drug Targeting: A New Approach in Locoregional Tumor Therapy with Chemotherapeutic Agents: Experimental Animal Studies, *Hno*, vol. 53, pp. 618–622, 2005.
3. H. Alimohamadi and M. Imani, Finite Element Simulation of Two-Dimensional Pulsatile Blood Flow thorough a Stenosed Artery in the Presence of External Magnetic Field, *Int. J. Comp. Meth. in Eng. Sci. and Mech.*, vol. 15, pp. 390–400, 2014.
4. L.E. Udrea, N.J. Strachan, V. Bădescu, and O. Rotariu, An In Vitro Study of Magnetic Particle Targeting in Small Blood Vessels, *Phys. in Medicine and Biology*, vol. 51, pp. 48–69, 2006.
5. M. Pinho, B. Brouard, J.-M. G  nevaux, N. Dauchez, O. Volkova, H. M  zi  re, and P. Collas, Investigation into Ferrofluid Magnetoviscous Effects under an Oscillating Shear Flow, *J. Magnetism and Magnetic Mat.*, vol. 323, pp. 2386–2390, 2011.
6. A. Nacev, C. Beni, O. Bruno, and B. Shapiro, The Behaviors of Ferro-magnetic Nano-particles in and around Blood Vessels under Applied Magnetic Fields, *J. Magnetism and Magnetic Mat.*, vol. 323, pp. 651–668, 2011.
7. S. Pal, A. Data, S. Sen, A. Mukhopdhyay, K. Bandopadhyay, and R. Ganguly, Characterization of a Ferrofluid-based Thermomagnetic Pump for Microfluidic Applications, *J. Magnetism and Magnetic Mat.*, vol. 323, pp. 2701–2709, 2011.
8. M. Hadavand, A. Nabovati, and A.C. Sousa, Ferrofluid Permeation into Three-Dimensional Random Porous Media: A Numerical Study Using the Lattice Boltzmann Method, *Transport in Porous Media*, pp. 1–16, 2013.
9. H. Alimohamadi, M. Imani, and M. Shojaeizadeh, Computational Analysis of Pulsatile Biofluid in a Locally Expanded Vessel under the Action of Magnetic Field, *Adv. in App. Sci. Res. J.*, vol. 4, pp. 96–103, 2013.
10. H. Aminfar, M. Mohammadpourfard, and F. Mohseni, Two-phase Mixture Model Simulation of the Hydro-thermal Behavior of an Electrical Conductive Ferrofluid in the Presence of Magnetic Fields, *J. Magnetism and Magnetic Mat.*, vol. 324, pp. 830–842, 2012.
11. R. Bali and S. Sharma, Effect of Magnetic Field in Lubrication of Synovial Joints, *Tribology Letters*, vol. 19, pp. 281–287, 2005.
12. H. Alimohamadi and M. Imani, Computational Analysis of Synovial Fluid in Actual Three Dimensional Modeling of Human Knee Joint under the Action of Magnetic Field, *Int. J. Energy and Tech.*, vol. 5, pp. 1–8, 2013.
13. A.D. Grief and G. Richardson, Mathematical Modelling of Magnetically Targeted Drug Delivery, *J. Magnetism and Magnetic Mat.*, vol. 293, pp. 455–463, 2005.

14. S. Chakravarty and S. Sen, Dynamic Response of Heat and Mass Transfer in Blood Flow through Stenosed Bifurcated Arteries, *Korea-Aust. Rheol. J.*, vol. 17, pp. 47–62, 2005.
15. E. Tzirtzilakis and V. Loukopoulos, Biofluid Flow in a Channel under the Action of a Uniform Localized Magnetic Field, *Comp. Mech.*, vol. 36, pp. 360–374, 2005.
16. L. Ai and K. Vafai, A Coupling Model for Macromolecule Transport in a Stenosed Arterial Wall, *Int. J. Heat and Mass Trans.*, vol. 49, pp. 1568–1591, 2006.
17. T. Streck and H. Jopek, Computer Simulation of Heat Transfer through a Ferrofluid, *Physica Status Solidi (b)*, vol. 244, pp. 1027–1037, 2007.
18. V. Rathod and S. Tanveer, Pulsatile Flow of Couple Stress Fluid through a Porous Medium with Periodic Body Acceleration and Magnetic Field, *Bull. Malays. Math. Sci. Soc.*, vol. 32(2), pp. 245–259, 2009.
19. J. Singh and R. Rathee, Analytical Solution of Two-dimensional Model of Blood Flow with Variable Viscosity through an Indented Artery Due to LDL Effect in the Presence of Magnetic Field, *Int. J. Phys. Sci.*, vol. 5, pp. 1857–1868, 2010.
20. E.A. Finol and C.H. Amon, Flow-induced Wall Shear Stress in Abdominal Aortic Aneurysms: Part I-Steady Flow Hemodynamics, *Comp. Meth. in Biomech. & Biomedical Eng.*, vol. 5, pp. 309–318, 2002.
21. E. Tzirtzilakis, A Mathematical Model for Blood Flow in Magnetic Field, *Physics of Fluids*, vol. 17, p. 077103, 2005.
22. Y. Cho and K. Kensey, Effects of the Non-Newtonian Viscosity of Blood on Flows in a Diseased Arterial Vessel. Part 1: Steady Flows, *Biorheology*, vol. 28, pp. 241–262, 1990.
23. F. Scarpa and F. Smith, Passive and MR Fluid-coated Auxetic PU Foam—mechanical, Acoustic, and Electromagnetic Properties, *J. Intelligent Mat. Sys. and Structures*, vol. 15, pp. 973–979, 2004.
24. S. Matsuo, M. Tsuruta, M. Hayano, Y. Imamura, Y. Eguchi, T. Tokushima, and S. Tsuji, Phasic Coronary Artery Flow Velocity Determined by Doppler Flowmeter Catheter in Aortic Stenosis and Aortic Regurgitation, *The Amer. J. Cardiology*, vol. 62, pp. 917–922, 1988.
25. H. Alimohamadi, M. Imani, and M. Shojaee-Zadeh, Non-Newtonian Blood Flow in Stenosed Artery with Porous Walls in the Presence of Magnetic Field, *Int. J. Tech. Enhancements and Emerging Eng. Res.*, vol. 2, pp. 69–75, 2014.